

RESEARCH ARTICLE

## Regulated exocytosis: renal aquaporin-2 3D vesicular network organization and association with F-actin

Mikkel R. Holst,<sup>1\*</sup> Louis G. Jensen,<sup>2\*</sup> Jesse Aaron,<sup>3</sup> Frédéric H. Login,<sup>1</sup> Sampavi Rajkumar,<sup>1,4</sup> Ute Hahn,<sup>2</sup> and Lene N. Nejsum<sup>1</sup>

<sup>1</sup>Department of Clinical Medicine, Aarhus University, Aarhus, Denmark; <sup>2</sup>Centre for Stochastic Geometry and Advanced Bioimaging, Department of Mathematics, Aarhus University, Aarhus, Denmark; <sup>3</sup>Advanced Imaging Center, Janelia Research Campus, Ashburn, Virginia; and <sup>4</sup>Department of Molecular Biology and Genetics, Aarhus University, Aarhus, Denmark

### Abstract

Regulated vesicle exocytosis is a key response to extracellular stimuli in diverse physiological processes, including hormone regulated short-term urine concentration. In the renal collecting duct, the water channel aquaporin-2 (AQP2) localizes to the apical plasma membrane as well as to small, subapical vesicles. In response to stimulation with the antidiuretic hormone, arginine vasopressin, aquaporin-2-containing vesicles fuse with the plasma membrane, which increases collecting duct water reabsorption and thus, urine concentration. The nanoscale size of these vesicles has limited analysis of their three-dimensional (3D) organization. Using a cell system combined with 3D superresolution microscopy, we provide the first direct analysis of the 3D network of aquaporin-2-containing exocytic vesicles in a cell culture system. We show that aquaporin-2 vesicles are  $43 \pm 3$  nm in diameter, a size similar to synaptic vesicles, and that one fraction of AQP2 vesicles localized with the subcortical F-actin layer and the other localized in between the F-actin layer and the plasma membrane. Aquaporin-2 vesicles associated with F-actin and this association were enhanced in a serine 256 phosphomimic of aquaporin-2, whose phosphorylation is a key event in antidiuretic hormone-mediated aquaporin-2 vesicle exocytosis.

AQP2; aquaporin-2; MDCK; superresolution; iPALM

### INTRODUCTION

Cellular responses to extracellular stimuli are mediated via different signaling cascades. Nevertheless, a fundamental response is regulated vesicle exocytosis that is conserved in hormone-regulated urine concentration, acidification of stomach contents, and neurotransmission. Signal-mediated vesicle exocytosis to the target plasma membrane alters the plasma membrane composition of ion and water channels and induces the secretion of signaling molecules.

Aquaporins (AQPs) are channel proteins that facilitate passive transport of water across biological membranes. In renal collecting ducts, urine concentration is fine-tuned by regulated exocytosis of small subapical AQP2 vesicles to the plasma membrane in response to circulating levels of the antidiuretic hormone arginine vasopressin (AVP) (1, 2). AVP binding to the AVP receptor (AVPR2) in the basolateral plasma membrane stimulates adenylate cyclase resulting in cAMP generation and activation of protein kinase A (PKA), which is thought to phosphorylate AQP2 on serine 256 (S256) in the COOH-terminal tail (3). At basal conditions, without AVP stimulation, some S256 phosphorylation was also observed (4). Besides S256, the COOH-terminal harbors three confirmed phosphorylation sites, namely, S261, S264, and S269 (5–8) [for recent reviews focusing on AQP2 phosphorylation and regulation (1, 9)].

Immunoelectron microscopy of vesicles in neuronal synapses and of AQP2 revealed that the size of exocytic vesicles is below the diffraction limit of light, and they localize close to the target plasma membrane with actin filaments (F-actin) (10–12). In contrast, the three-dimensional (3D) organization of regulated exocytic vesicles has been generally limited to light microscopy and is poorly understood. Here, we circumvented these indirect and low-resolution methods by utilizing recent advances in 3D superresolution microscopy [interferometric photoactivated localization microscopy (iPALM) (13, 14)] that enable imaging of the nanospatial organization of vesicular populations in cells at a resolution down to 20 nm in the *xy*-axis (lateral) and 10–15 nm in the *z*-axis (vertical).

### MATERIALS AND METHODS

All reagents were purchased from Merck unless otherwise stated.

#### DNA Preparation

The mEOs3.2-AQP2 constructs were generated by swapping the pPAGFP (PhotoActivatable Green Fluorescent Protein) coding sequence of the pPAGFP-AQP2 plasmids (7) with the mEOs3.2 coding sequence. The mEOs3.2 sequence

\* M. R. Holst and L. Gammelgaard contributed equally to this work.  
Correspondence: L. N. Nejsum (nejsum@clin.au.dk).  
Submitted 28 June 2021 / Revised 11 August 2021 / Accepted 11 August 2021



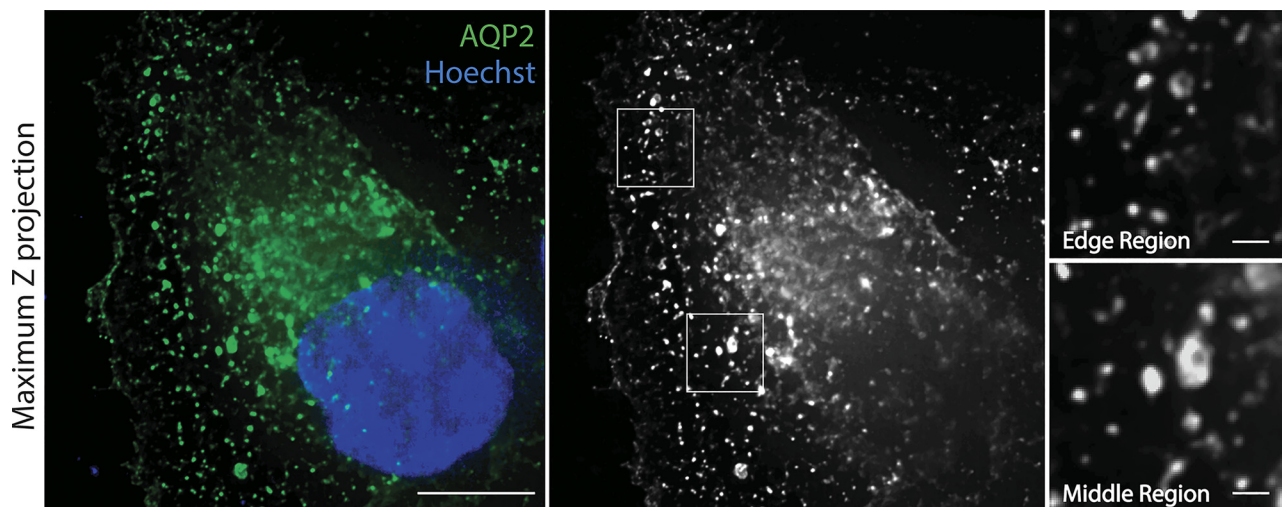


**Figure 1.** Localization of endosomal AQP2 by ExM. Cells stably expressing AQP2 were seeded on glass, fixed, stained with antibodies against AQP2 and Hoechst. Cells were estimated to be expanded 4.5 $\times$ . This was estimated by measuring nuclei length and comparing expanded with nonexpanded cell nuclei. The expansion enabled imaging in  $x$ - $y$  with a resolution  $\sim$ 45 nm/pixel. Scale bar in left micrograph is 5  $\mu$ m and 500 nm in right insets. AQP2, aquaporin-2; ExM, expansion microscopy.

was amplified using the mEos3.2-C1 plasmid as template and the following primers: forward 5'-CATCAAGTGATCATA-TGCCAAG and reverse 5'-caagacgtcgactccggatcgtctggcattgtc. The PCR product and the different pPAGFP-AQP2 plasmids were digested with NdeI and SalI restriction enzymes (Thermo Fisher Scientific). The digested plasmids (lacking the pPAGFP sequence) were ligated with mEos3.2. All sequences were verified by sequencing (Eurofins GATC,

Cologne, Germany). cDNA encoding mEos3.2-C1 was a kind gift from Michael Davidson and Tao Xu (Addgene plasmid No. 54550; <http://n2t.net/addgene:54550>).

#### Cell Culture and Setup for Microscopy

FTM-AQP2 cells (15, 16) were grown at 5% CO<sub>2</sub> and 37°C in Dulbecco's modified Eagle medium with 1g/L D-glucose (DMEM, Gibco), 10% fetal bovine serum (FBS, Gibco), 5  $\mu$ g/

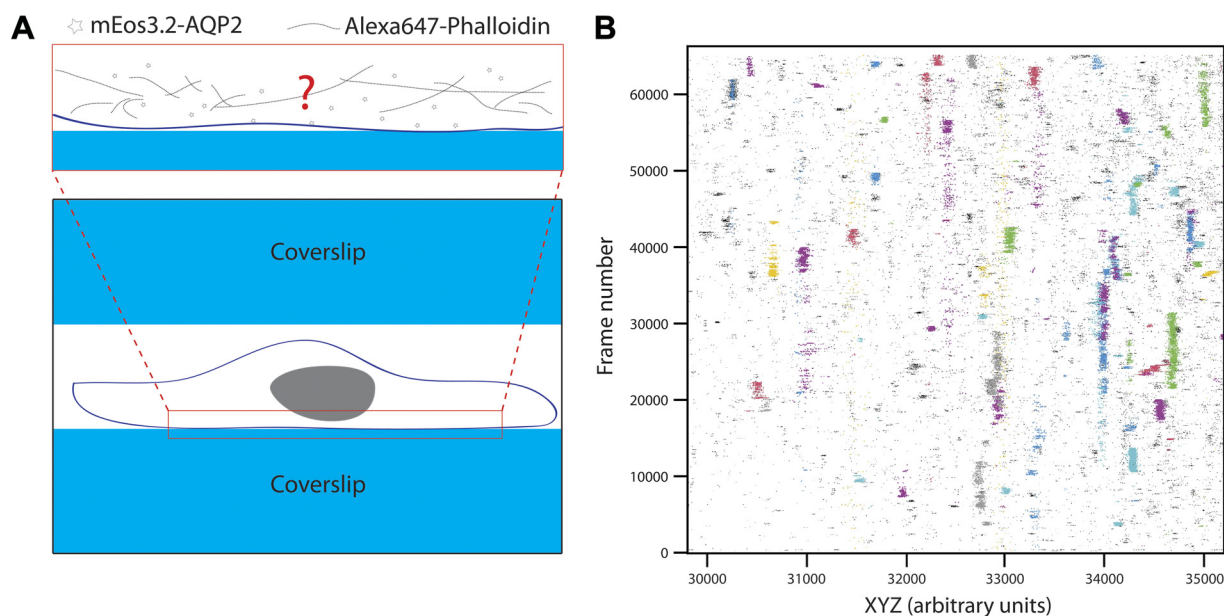
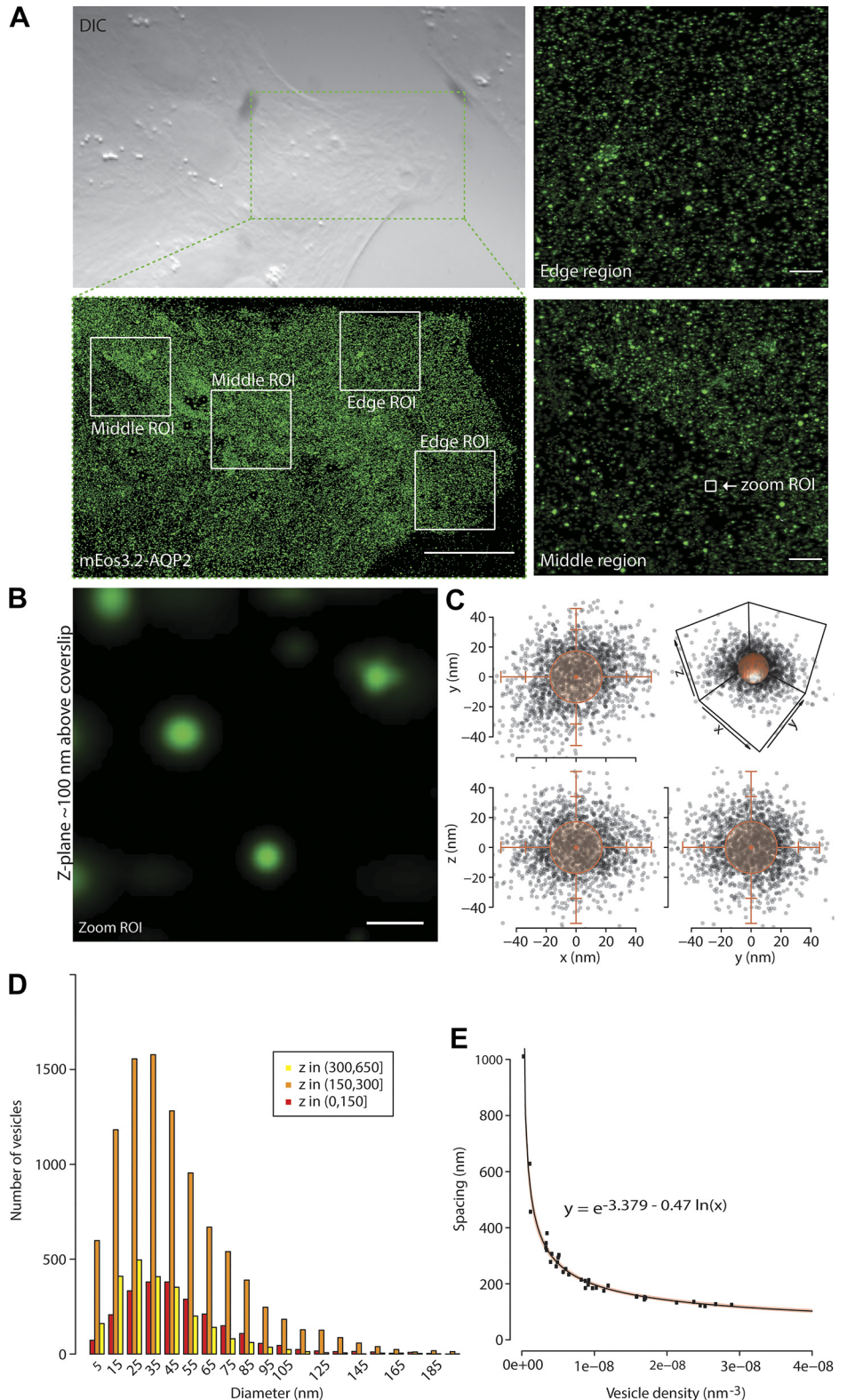


**Figure 2.** Setup of iPALM sandwich imaging chamber and spatiotemporal signal output. **A:** cells were grown on 18-mm coverslips coated with 100-nm gold bead fiducials. After fixation and labeling, cells were placed in chambers assembled from the 18-mm cell-containing fiducial cover glass, 5-min epoxy (ITW Performance Polymers) and Vaseline (Unilever), emerged with PHEM buffer (60 mM Pipes, 25 mM Hepes, 10 mM EGTA, 2 mM MgCl<sub>2</sub> pH 6.9) and a 25-mm cover glass on top. Imaging chamber was loaded into the microscope and objectives were aligned before iPALM. Cells with a medium expression of mEos3.2-AQP2 signal were chosen for imaging. iPALM imaging area is indicated by the red rectangle. **B:** sideview of a region of interest shows the spatiotemporal imaging behavior of detected signal points in a representative ROI. Colored points correspond to the detected groups posited to be vesicles, whereas black points were considered background and omitted from analysis. The dense clustering structure observed in time indicates an unusually large amount of fluorescent activity in these groups, which may be the result of atypical blinking behavior in tightly packed, fluorescing probes. AQP2, aquaporin-2; iPALM, interferometric photoactivated localization microscopy; ROI, region of interest.

mL Blasticidin S HCL (Gibco), and 100 µg/mL Hygromycin B (Invitrogen). Cells do not express endogenous AQP2. Cells were induced with 10 ng/mL doxycycline to express AQP2, AQP2-S256A, or AQP2-S256D and transiently transfected to express low levels of mEos3.2-tagged AQP2 and phosphomu-

tants 24 h before fixation. Expression levels were kept low to avoid artifacts from overexpression. Cells were transiently transfected with a mixture of 0.5-µg cDNA constructs and 10-µg sheared salmon sperm DNA (Cat. No. AM9680, Thermo Fisher Scientific) using a Genepulser Xcell (Biorad) for

**Figure 3.** iPALM localization of AQP2 to small vesicles close to the plasma membrane (PM). **A:** *top left*, differential interference contrast (DIC) image of subconfluent cell monolayer and lower left maximum projected micrograph of iPALM renderings of MDCK cells expressing mEos3.2-AQP2 and untagged AQP2 (scale bars 10 µm). *Top and bottom right* maximum projected images show examples of regions of interest chosen for analysis (scale bars 1 µm). **B:** *right* image shows the zoom ROI from *bottom right* image (A) of a Z-layer with spherical clusters positioned close to the PM (scale bar 100 nm). **C:** clusters found using the density-based spatial clustering of applications with noise (DBSCAN) algorithm were fitted to a model assuming AQP2 on spherical vesicles observed with noise. The shaded circle/sphere indicates the estimated vesicle. The bars extending from the sphere surface indicate 1 and 2 times the standard deviation of the location uncertainty in the given direction. **D:** the distribution of wild-type (WT) vesicle diameters for different sections of depth into the cell.  $N = 14,448$ ; Type = diameter of detected WT vesicles across all WT ROI. **E:** the distance between one vesicle to the nearest other vesicle, as a function of the number of vesicles per  $\text{nm}^3$ .  $N = 38$ ; Type = average nearest vesicle-to-vesicle distance for each ROI, for each of the 76 ROI. For each cell, the 2 regions corresponding to the same condition (middle vs edge) were then averaged together, thus we have  $38 = 76/2$  points. Model = mixed effects linear model on the log-log scale. Random effects term for data points coming from the same cell (pairwise observations). The shaded area indicates a 95% confidence global envelope. AQP2, aquaporin-2; iPALM, interferometric photoactivated localization microscopy; MDCK, Madin–Darby canine kidney cells; ROI, region of interest.



electroporation according to the manufacturer guidelines. After electroporation, cells were seeded out on 25-mm diameter, No. 1.5 thickness glass coverslips containing gold nanorod fiducial markers (Cat. No. A12-40-600, Nanopartz, Inc.). Cells were fixed at room temperature with cytoskeleton fixation buffer containing 10 mM MES, 3 mM MgCl<sub>2</sub>, 138 mM KCl, 2 mM EGTA, 0.32 M sucrose (pH 6.1), and 4% PFA for 20–25 min. Cells were permeabilized for 10 min with 0.1% Triton X-100 in blocking buffer containing 3% BSA in PBS, washed, and placed in blocking buffer for 20 min. Cells were then stained with 1:200 Alexa647-phalloidin for 30 min. After fixation and staining, cells were immersed in dSTORM buffer [3] containing 50 mM Tris (pH 8), 10 mM NaCl, 100 mM mercaptoethanol amine, 0.5 mg/mL glucose oxidase, and 0.03 mg/mL catalase (all from Sigma). An 18-mm diameter, No. 1.5 thickness coverslip was adhered atop the fiducial-containing coverslip with epoxy and sealed.

### Expansion Microscopy

Expansion microscopy (ExM) was performed as previously described with minor modifications (17, 18). FTM-AQP2 cells (15, 16) were seeded on 22 × 22 mm collagen-coated coverslips. After 24 h, AQP2 expression was induced with 10 ng/mL doxycycline and cells were also incubated with 50 μM indomethacin for 24 h. Cells were washed 3× in PBS and fixed for 10 min with 4% PFA solution at room temperature (RT). Next, cells were permeabilized with 0.1% Triton X-100 + 3% BSA in PBS for 10 min. Cells were blocked in 3% BSA in PBS for 30 min and incubated with primary antibody (mouse anti-AQP2 antibody, Cat. No. sc-515770, Santa Cruz Biotechnology, 1:20) in 3% BSA

in PBS for 1 h. Cells were washed and incubated with secondary antibody (Dylight-594, donkey-anti-mouse, ImmunoReagents Inc., 1:100) in 3% BSA in PBS for 1 h. After wash in PBS, cells were postfixed with 0.25% glutaraldehyde in PBS for 10 min. After PBS wash, cells were incubated with 100-μL monomer solution 8.1% Na acrylate (Cat. No. 408220, Sigma), 2.66% wt/vol acrylamide (Cat. No. A9099, Sigma), 0.32% wt/vol N,N'-methylenebisacrylamide (Cat. No. M7279, Sigma), 11.2% NaCl wt/vol, in PBS for 1 h at RT. The coverslip was placed upside down on a drop of 190-μL gelation solution [10 μL of 10% vol/vol tetramethylenediamine (TEMED) (Cat. No. T7024, Sigma) and 10 μL of 10% wt/vol ammonium persulfate (APS) (Cat. No. A3678, Sigma) was added to 480 μL of monomer solution] and incubated for 1 h at RT. Subsequently, digestion was performed for 1 h at 37°C [0.5% Triton X-100, 0.8 M guanidine HCl (Cat. No. 50-01-1, Sigma), 8 U/mL proteinase K in TAE buffer]. The gel was cut into a smaller piece and placed into 3 mL of Milli-Q water in a 6-well plate and incubated overnight at 4°C. The next day, the water was replaced and the gel was incubated for 30 min at RT with gentle shaking. This was repeated and subsequently, the Milli-Q water was removed, and the gel was incubated with fresh Milli-Q water containing Hoechst (1:500) for 30 min. The gel was washed in Milli-Q water for 30 min, placed in an imaging chamber, and imaged on a Nikon Eclipse Ti-E system equipped with a ×100 1.45 NA objective and a Zyla sCMOS camera, controlled by NIS Elements from Nikon. The fluorescence illumination system was CoolLED-pE-300<sup>white</sup>. Fluorescence filter sets for DAPI and TexasRed were used to detect Hoechst and Dylight-594, respectively. Images were deconvolved with Huygens Software (Scientific Volume Imaging, the Netherlands, <http://svi.nl>).

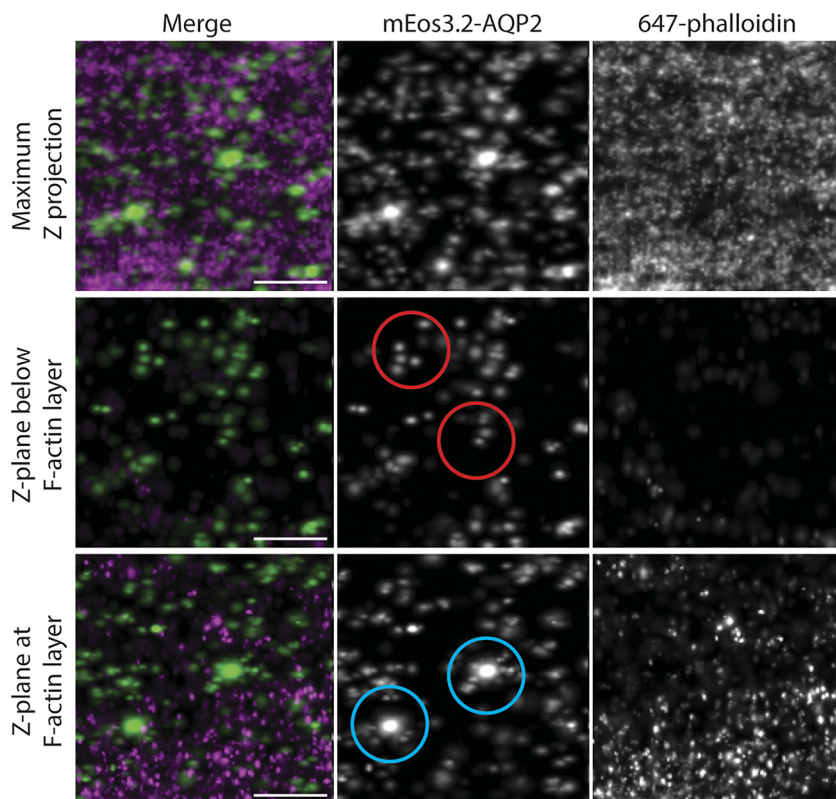
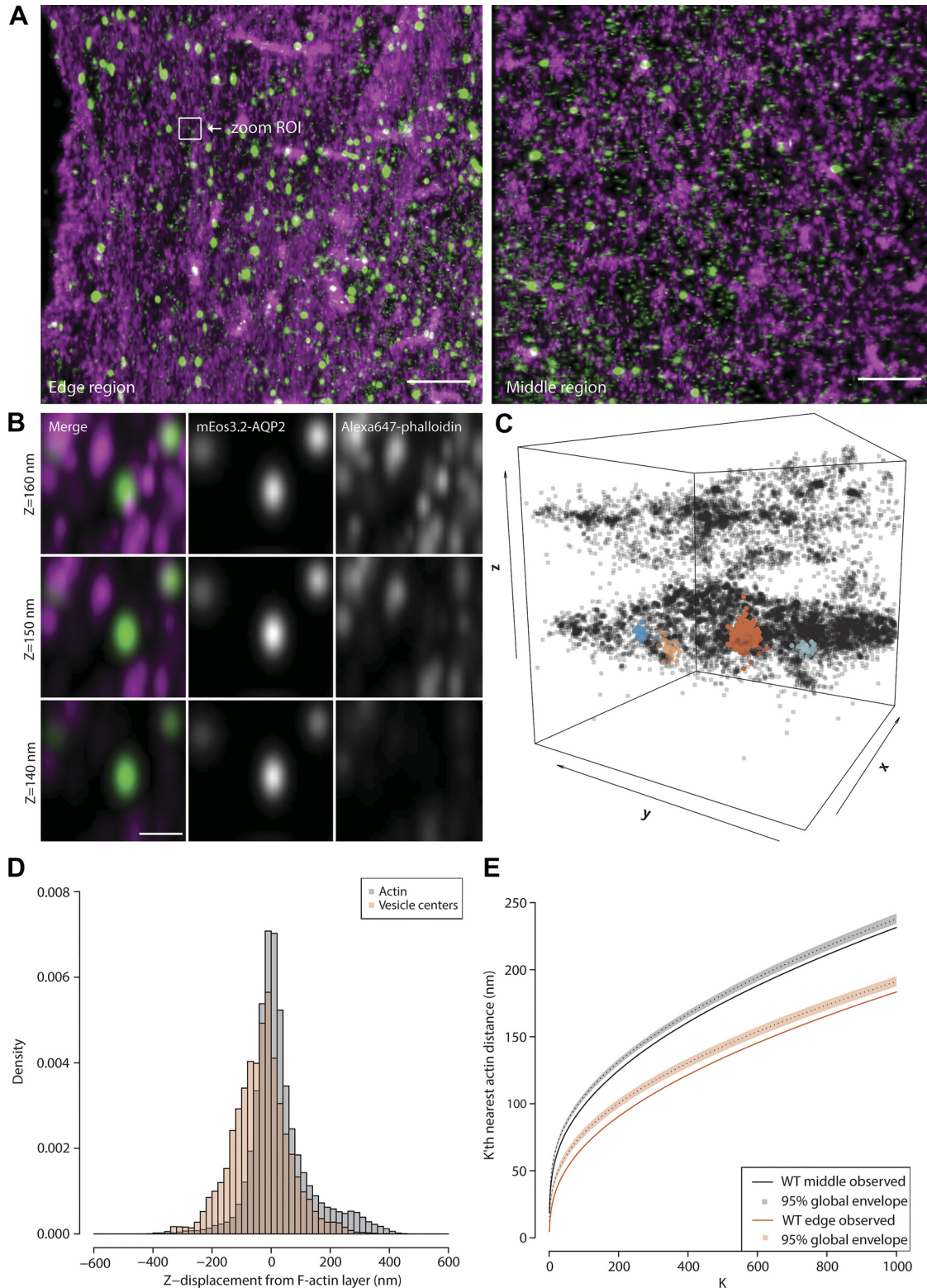


**Figure 4.** iPALM positions AQP2 in spherical vesicles and larger endosomes close to the F-actin layer. Representative iPALM renderings of MDCK cells expressing mEOS3.2-AQP2 and untagged AQP2 (green), stained with phalloidin-647 to label actin (magenta). Small spherical vesicles were localized between the plasma membrane and the F-actin layer (red circles). At the F-actin layer, AQP2 localizations also draw a positioning in endosome-like organelles (blue circles). Scale bars 1 μm. AQP2, aquaporin-2; iPALM, interferometric photoactivated localization microscopy; MDCK, Madin–Darby canine kidney cells.

**Imaging**

Samples were imaged using interferometric photoactivation localization microscopy (iPALM), as described previously (14, 19). Samples were placed in the iPALM and sequentially

illuminated in total internal reflection fluorescence (TIRF) mode with 640- and 561-nm diode lasers, respectively (Opto Engine) through a  $\times 60$  APO TIRF, 1.49NA objective (Nikon) at 1–3  $\text{kW}/\text{cm}^2$  irradiance. mEos molecules were photoconverted using ca.  $1\text{W}/\text{cm}^2$  405-nm laser illumination (Coherent). The



405-nm laser power was adjusted to ensure that only a small fraction of photoconverted mEos3.2 blinked in each image. For each cell, 50,000–75,000 fluorescence images were captured per channel at 30- to 50-ms exposure time, through a 647-nm longpass filter (Semrock) for Alexa Fluor 647 images, or a  $593 \pm 20$ -nm bandpass filter (Semrock) for mEos images, onto 3 EM-CCD detectors (iXon, Andor Technology Ltd.). The different channel data sets were aligned using fiducial markers, consisting of gold nanorods (40-nm long axis diameter, 25-nm short axis diameter from Nanopartz, Inc.). Typical alignment accuracies are on the order of the localization precision ( $\sim 20$  nm) (20).

## Analysis

Single fluorophores were localized in  $x$ ,  $y$ , and  $z$  dimensions, and images were rendered using the PeakSelector software (Janelia Research Campus). The analyzed data consist of 76 regions of interest (ROI), coming from a total of 19 unique cells. From each cell, four ROIs were cropped out: two from a central site in the cell and two from an edge site. The number of cells corresponding to different degrees of phosphorylation [wild-type (WT), alanine (A), aspartic acid (D)] was spread over three independent experiment days, respectively (3, 6). Regions coming from the same site type in the same cell were treated as a single region by taking averages of any statistics computed on them.

For detection of AQP2 clusters (used interchangeably with “vesicles” below), the density-based spatial clustering of applications with noise (DBSCAN) algorithm (11) was employed, with parameter choices  $\text{MinPts} = 10$  and  $\text{Eps} = 50$  nm. Eps was chosen relatively large to account for the scale of localization uncertainty. Results were not sensitive to these choices for sensible parameter values, due to the large degree of spatial separation of vesicles, relative to their size. The vesicles thus found were modeled as proteins lying on the surface of a hollow sphere following a von Mises–Fisher distribution, observed with Gaussian noise added to each point. The covariance matrix of the noise added to each point in the vesicle was estimated automatically by PeakSelector as part of the localization routine and was used in place of the true covariance matrix when estimating vesicle parameters, which was done by maximum likelihood. In this manner, we obtain estimates of the vesicle centers and diameters.

Analysis of AQP2 vesicle characteristics, such as their diameter and association with nearby actin, was carried out by first computing a statistic of interest on each vesicle, and then averaging over the vesicles sharing ROI. Linear mixed effects

models (21) were used for summarizing results across different ROIs, and model assumptions were checked by residual tests. All models included a random effect shared for the ROIs coming from the same cell and fixed effects for the degree of phosphorylation and the ROI cell site (central/edge).

For investigation of colocalization between AQP2 and actin, we first considered if there was significant statistical association for S256-WT. For each ROI, AQP2 vesicle centers were computed and overlaid on actin. The centers demonstrated spatial stationarity in the  $XY$ -plane, but not in the  $Z$ -plane. For this reason, we tested for significant association using shift in the  $XY$ -plane only. This was accomplished by a random superposition hypothesis test, based on distances to the 1,000 nearest neighboring (NN) actin proteins from vesicle shells. To investigate if the degree of colocalization differs based on phosphorylation status, we similarly computed the distances to the 1,000 NNs for the S256-A- and S256-D-type ROIs. For an overall test of differences between mutant types, we modeled the mean distance of these 1,000 NNs. Additional tests at each of the  $k$ th nearest actin proteins was done analogously and summarized graphically. We look at the 1,000 NNs, as opposed to the raw number of actin molecules within a set of ranges, because the NNs lend themselves more easily to statistical modeling. In addition, the raw number of molecules is significantly more affected by outlier behavior, and a single actin fiber passing close to a vesicle may exhibit 100- or even 1,000-folds of artificially increased association scores when compared with the typical vesicle; this effect is much less pronounced for NN distances. The specific choice to look at 1,000 NNs was made primarily so as to correspond to a relevant range of interactions, which in turn depends on the expected range of interactions, protein expression levels, and some additional range to account for noisy observations. The 1,000 NNs here correspond to looking at interactions with actin structures primarily in the 0- to 300-nm distance range, which allows us to look for both very close interactions and also any indirect interactions mediated by unseen structures. Additionally, by looking at a large number of NNs, we obtain a mean distance that is less influenced by the uncertainty in both protein localizations and vesicle parameters.

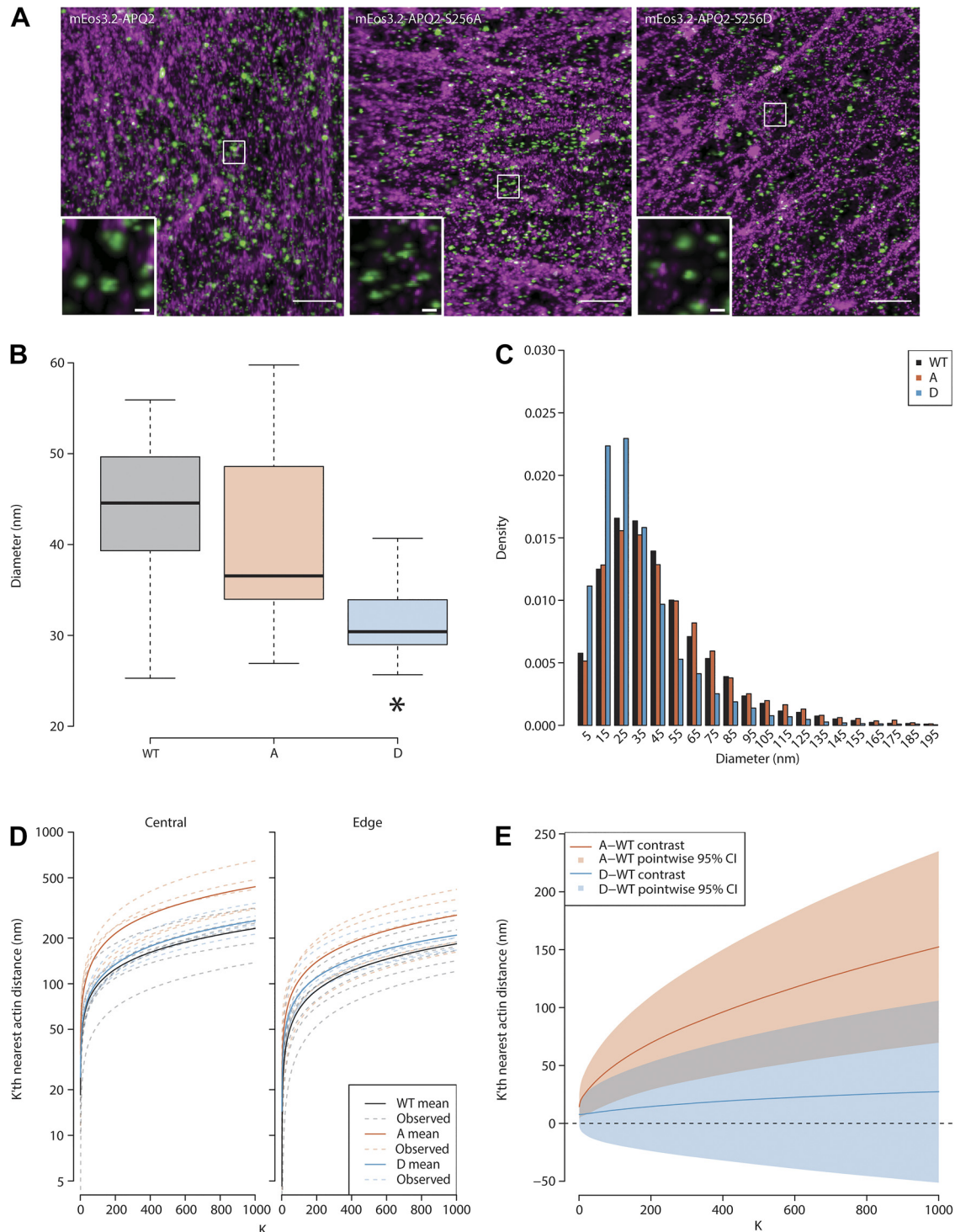
## RESULTS AND DISCUSSION

We used our previously described cell system, FTM-AQP2 cells, where AQP2 is expressed in Madin–Darby canine kidney (MDCK) cells under the control of a doxycycline inducible promoter (15, 16). In subconfluent FTM-AQP2 cells, AQP2

**Figure 5.** AQP2 is positioned in vesicles between the plasma membrane (PM) and the F-actin layer. *A*: representative iPALM renderings of MDCK cells expressing mEos3.2-AQP2 and untagged AQP2 (green), stained with phalloidin-647 to label F-actin (magenta) (scale bars 1  $\mu\text{m}$ ). *B*: examples of  $Z$ -layers with spherical clusters positioned between the PM and the F-actin layer (scale bar 100 nm). *C*: a small, typical cross section of actin (black points) and the vesicles found using density-based spatial clustering of applications with noise (DBSCAN) (colored points). F-actin is seen located primarily as a layer structure, and AQP2 localizes in close proximity to this layer. AQP2 locations considered as noise by the DBSCAN algorithm are not shown. *D*: the  $z$  coordinates of actin and AQP2 vesicle centers, relative to the F-actin layer position. The actin layer position was found as the  $z$  coordinate with maximal actin density.  $N = 18,340,907$  ACT localizations, 14,448 AQP vesicles; Type =  $Z$ -coordinates of individual ACT molecules and AQP vesicle centers across all 76 ROI. *E*: the distance from vesicle shells to the  $k$ th nearest F-actin location was computed, and the resulting neighbor curve was used as a means for quantifying the spatial relations between AQP2 vesicles and actin. This was done both for central (gray) and edge (red) parts of cells. As a test for colocalization, AQP2 vesicles were shifted relative to F-actin in the  $XY$ -plane, and the neighbor curves were again computed. Based on 500 shifts, a global envelope test was performed, yielding a region within which the curve would have to lie, assuming independence of AQP2 and actin. The curve lying outside and under the envelope indicates closer AQP2-to-actin distances than would be expected under independence.  $N = 14$  total, corresponding to 7 edge and 7 middle pairs of ROIs; Type = average distance from vesicle shells to  $k$ -nearest ACT for WT cells. Each of the 7 WT cells have 2 ROIs of the same type, which are averaged, and thus there are a total of 14 data points. Model = random superposition hypothesis. Tested using 500 random shifts with torus correction, and a global envelope test. AQP2, aquaporin-2; iPALM, interferometric photoactivated localization microscopy; MDCK, Madin–Darby canine kidney cells.

has been shown to shuttle to and from the plasma membrane in response to increased levels of cAMP (15), the main signaling downstream of AVP. Using conventional microscopy, only the larger endosomes can be imaged. To first confirm localization of AQP2 in vesicular membranes in large and smaller endosomes, we employed expansion microscopy (ExM) (17), which expands the sample 4.5× in each direction ( $x, y, z$ ) thus increasing resolution from 250 to ~70 nm allowing improved visualization of endosomal structures. ExM

confirmed that AQP2 localized in membranes of vesicle structures of different sizes distributed throughout the cell cytoplasm (Fig. 1). To image the smaller AQP2 exocytic vesicles close to the plasma membrane, we employed 3D superresolution imaging using the iPALM imaging system (imaging setup in Fig. 2A). For a detailed description of iPALM, we refer to Refs. 14 and 19. We used the cell setup in combination with transiently transfected AQP2 tagged with mEos3.2, a photoconvertible green/yellow fluorescent protein.



Since AQP2 tagged with a fluorescent protein has a tendency to aggregate, mEos3.2-AQP2 was expressed at low levels to ensure approximately one tagged monomer per tetramer (referred to hereafter as AQP2), which has been shown to prevent aggregation of the AQP2 tetramer thus enabling imaging with fluorescently tagged AQP2 (15, 22). Furthermore, F-actin has been suggested to form a barrier between AQP2 vesicles and the plasma membrane (23–25) but it has never been possible to obtain insight from cell cultures of the actual positioning of vesicles in respect to the F-actin layer at this close localization to the plasma membrane. To enable imaging of F-actin in conjunction with AQP2 vesicles, we used Alexa647-labeled phalloidin, which labels F-actin.

For each cell, 50,000–75,000 iPALM images were captured and  $x, y, z$  coordinates of single AQP2 proteins were determined. For analysis, we employed statistical methods for spatial point patterns to analyze the shape, size, and spacing of AQP2-containing vesicles. To ensure we were imaging whole vesicles in the cytoplasm, and not vesicles undergoing scission or fusion with the basal plasma membrane, nor microdomains in the basal plasma membrane, we used the coverslip as a reference zero point and performed vesicle analysis in the niche 100–400 nm above the coverslip (imaging setup in Fig. 2A). The imaging revealed a network of AQP2 clusters (Fig. 3, A and B and Supplemental Movie S1, see <https://doi.org/10.6084/m9.figshare.14854083>), which we modeled as proteins lying on the surface of hollow spheres (similar to vesicles) observed with noise (Fig. 3C). The AQP2 vesicle diameters had a right-skewed distribution, with diameters as large as 200 nm being observed in rare instances (Fig. 3D). The average AQP2 vesicle diameter was  $43 \pm 3$  nm, and vesicles were spaced apart with an average distance of  $197 \pm 60$  nm (Fig. 3E). Fewer, larger vesicles resembling recycling endosomes were also observed (Fig. 4). The analysis showed that the  $z$ -range with the largest vesicle population was positioned 150–400 nm from the coverslip. Our results support that AQP2 vesicles have similar sizes to that of presynaptic vesicles (26) but have smaller sizes compared with the larger diameter of transport vesicles in the secretory pathway and endocytic vesicles (reviewed in Ref. 27).

We examined the blinking behavior of mEos3.2-AQP2 in samples imaged with the iPALM system. As expected, we

noted areas of high localization density, which corresponded to putative vesicles. For each cell, 50,000–75,000 fluorescence images were captured and interestingly, the observed blinks of mEos3.2-AQP2 tended to be temporally clustered, rather than appearing randomly throughout the acquisition time, as shown in Fig. 2B. We speculate that this unexpected behavior may be due to a self-activation mechanism, either due to the high fluorophore density or the fact that AQP2 exists as tetramers or both. However, as shown in the plot in Fig. 2B, the localization density in these areas cannot be solely attributed to abnormally long on-times of the mEos3.2. Analysis of this plot indicates an average “on-time” of blinking mEos3.2-AQP2 of 66 ms (or  $\sim 1.3$  frames) within these areas.

Next, we imaged F-actin, which revealed a dense layer of F-actin in the cytoplasm  $\sim 200$  nm distal to the basal plasma membrane (Fig. 5, A–C). The majority (66.91%) of AQP2 vesicles were positioned between the plasma membrane and the dense F-actin layer (Fig. 5D and Supplemental Movie S2, see <https://doi.org/10.6084/m9.figshare.14854080>) indicating that the F-actin layer did not compose a physical barrier toward the plasma membrane for this fraction of AQP2 vesicles. To tests in 3D if AQP2 vesicles associate with F-actin or if the proximity is random, we examined the spatial relationship of AQP2 vesicles with F-actin using a Monte Carlo test for independence of localizations. The distance from each AQP2 vesicle shell to the nearest 1,000 neighboring (NN) F-actin localizations in central and peripheral regions of cells was computed, as was a mean-curve for all vesicles. We first assumed distributional invariance of AQP2 vesicle centers under shifts in the  $XY$ -plane and then simulated new mean-curves from the null hypothesis of independence by randomly shifting AQP2 vesicles in  $XY$ , while keeping  $Z$ -coordinates for AQP2 fixed and  $XYZ$ -coordinates for F-actin fixed. Based on the simulated curves, we performed a global envelope test based on extreme rank lengths (20). The observed mean-curves for central and edge regions of the cells were both entirely outside their respective envelopes indicating AQP2-to-F-actin distances that were shorter than expected if they were independent of each other (Fig. 5E,  $P_{\text{val}} = 0.002$ ). Thus, the analysis revealed an association between AQP2 vesicles and F-actin (Fig. 5, A–C).

**Figure 6.** Phosphorylation of AQP2 at S256 affects vesicle size and F-actin association. A: representative iPALM renderings of MDCK cells expressing mEos3.2-AQP2 (left), mEos3.2-AQP2-S256A and untagged AQP2-S256A (middle) and mEos3.2-AQP2-S256D and untagged AQP2-S256D (right). All stained with Alexa647-phalloidin to label F-actin (scale bars 1  $\mu\text{m}$ ). The inset zooms show localizations in  $Z$ -layers under the F-actin layer (scale bars 100 nm). B: the average vesicle diameter in each data region was used for modeling the mean vesicle diameter size as a function of the cell type. Number of data regions were 14, 10, and 12 for AQP2, AQP2-S256A, and AQP2-S256D, respectively. Diameters were compared using  $F$  tests, with the Kenward–Roger approximation to the degrees of freedom.  $N = 38$  total, corresponding to (14, 12, 12) respectively for [wild-type (WT), alanine (A), aspartic acid (D)]; Type = average diameter of vesicles coming from the same ROI, for each of the 76 ROI. For each cell, the 2 regions corresponding to the same condition (middle vs edge) were then averaged together, thus we have  $38 = 76/2$  points. Model = mixed effects linear model with random effects term for regions coming from the same cell. C: the distribution of observed vesicle diameters across all data regions, for each cell type.  $N = 35,922$  total, corresponding to (14,448, 10,230, 11,244) respectively, for (WT, A, D); Type = diameter of vesicles across all 76 ROI. D: neighbor graphs computed for each cell and region type, shown on a log-scale. Full lines indicate the mean curves across regions, and dashed lines are curves from individual data regions. The average distance from a vesicle shell to its nearest 1,000 actin neighbors was used as a statistic for comparing the degree of association. These distances were compared using  $F$  tests, with the Kenward–Roger approximation to the degrees of freedom. \*indicates significance.  $N = 38$  total, corresponding to (14, 12, 12), respectively, for WT, A, D; Type = average distance from vesicle shells to  $k$ -nearest ACT for all cells, separated according to middle/edge region type. Each of the cells have 2 ROIs of the same type, which are averaged, and thus there are a total of 38 data points. Model = linear mixed effects model with random effects term for observations from the same cell. E: the distance to the  $k$ th nearest actin location from vesicle surfaces was modeled as a function of cell type, and mean contrasts with WT were estimated. Pointwise confidence intervals were computed for each  $k$  between 1 and 1,000. These provide a visual description of whether cell mutants are differently, or similarly, associated with actin for varying spatial proximity. AQP2, aquaporin-2; iPALM, interferometric photoactivated localization microscopy; MDCK, Madin–Darby canine kidney cells.

Our results indicate that small AQP2 transport vesicles associate with F-actin and localize both with the F-actin layer distal to the plasma membrane and between the F-actin layer and proximal to the plasma membrane.

AVP binding to the AVP receptor elicits signaling cascades that culminate in phosphorylation of several residues in the AQP2 COOH-terminal tail and subsequent fusion of AQP2 vesicles with the plasma membrane (PM) (recently reviewed in Refs. 1 and 9). AQP2 serine 256 (S256) phosphorylation downstream of AVP is a key event and precedes phosphorylation of the other serines (28). S256 phosphorylation can be mimicked by the AQP2-S256D mutation and its nonphospho-mimic by AQP2-S256A. The diameter of AQP2-S256A vesicles ( $41 \pm 4$  nm) was similar to AQP2-wt vesicles ( $P_{\text{val}} = 0.718$ ; Fig. 6, A–C), whereas AQP2-S256D ( $31 \pm 4$  nm) vesicles were significantly smaller ( $P_{\text{val}} = 0.022$ ). Spacing between vesicles was not significantly different between AQP2-wt, AQP2-S256D, and AQP2-S256A ( $P_{\text{val}} = 0.06096$ ) in the cell center or periphery ( $P_{\text{val}} = 0.60049$ ), when controlling for the number of vesicles per  $\text{nm}^3$ .

Next, we examined the distribution of AQP2-S256D and AQP2-S256A vesicles in relationship to F-actin (Fig. 6D). In the peripheral cytoplasm, AQP2-S256A vesicles were less associated with F-actin than AQP2-wt with a 58% larger distance between vesicles and the nearest 1,000 neighboring F-actins ( $P_{\text{val}} = 0.011$ ). AQP2-S256D vesicles were 11% farther from F-actin than AQP2-wt, but this was not significantly different ( $P_{\text{val}} = 0.531$ ). In the central cytoplasm, AQP2-S256A vesicles were localized 86% ( $P_{\text{val}} < 0.001$ ) farther from F-actin than AQP2-wt vesicles, whereas AQP2-S256D had a similar distance to F-actin as AQP2-wt ( $P_{\text{val}} = 0.356$ ), indicating that nonphosphorylated AQP2 on S256 is less associated with F-actin than AQP2 phosphorylated on S256. These results suggest that in this cell system, phosphorylation of AQP2 at S256 regulates the size of AQP2 vesicles and their association with F-actin both in the central and peripheral region of the cell.

Previous studies reported that global F-actin depolymerization results in AQP2 targeting to the plasma membrane (23, 25, 29), but it was unknown whether the F-actin layer constitutes a physical barrier between AQP2 vesicles and the plasma membrane and/or facilitates AQP2 vesicle delivery to the plasma membrane upon AQP2 S256 phosphorylation (21). We found a large fraction of AQP2 vesicles in the niche between the F-actin layer and the plasma membrane. Thus, a possible scenario is that these AQP2 vesicles may be mobilized for exocytosis on increases in circulating AVP without disassembly of the F-actin layer, thereby ensuring a rapid exocytic response. The remaining vesicles, which localize with the F-actin layer, as well as AQP2 stored in larger endosomes further inside the cell may be dependent on dissociation of the F-actin layer for AQP2 plasma membrane targeting on AVP stimulation.

Also, our results support a model where association of AQP2 vesicles with F-actin is enhanced on AQP2 S256 phosphorylation. Thus, we hypothesize that near the plasma membrane, S256 phosphorylation increases the propensity for vesicle accumulation with F-actin, and thus, the likelihood of vesicle fusion with the plasma membrane. AQP2-wt and AQP2-S256D vesicles may have similar transport capacities along F-actin tracks, but

differences in their plasma diffusion coefficients (22) and endocytosis rates (30) may result in an increased plasma membrane localization of AQP2-S256D compared with AQP2-wt.

Regulated vesicle exocytosis is a conserved response to many extracellular signals that result in the acidification of stomach contents, neurotransmission, and hormone-regulated urine concentration. Detailed analysis of these vesicles and F-actin has focused on the neuronal synapse, where specialized  $\sim 40$ -nm vesicles associate with F-actin close to the plasma membrane at the synaptic cleft (12, 26). Our analysis of the spatial organization and physical associations of AQP2 vesicles with F-actin is the first direct analysis of a 3D network of exocytic vesicles in a nonneuron cell type and reveals striking similarities with synaptic vesicles in size. Future studies may reveal if different signal-mediated vesicle exocytosis pathways have conserved mechanisms and organizations.

## DATA AVAILABILITY

All data, code, and materials used in the analysis is available in some form on request to any researcher for purposes of reproducing or extending the analysis.

## SUPPLEMENTAL DATA

Supplemental Movie S1: <https://doi.org/10.6084/m9.figshare.14854083>.

Supplemental Movie S2: <https://doi.org/10.6084/m9.figshare.14854080>.

## ACKNOWLEDGMENTS

We are grateful to data scientist Eric Wait and to technical coordinator Satya Khuon, Advanced Imaging Center, Janelia Research Campus, USA, for technical suggestions regarding data analysis and technical assistance, respectively.

Present address of M. R. Holst: Dept. of Biomedicine, Aarhus University, 8000 Aarhus C, Denmark.

## GRANTS

This project was supported by the Independent Research Fund, Denmark Grant DFF 4181-00379B, Aarhus University Research Foundation (AUFF) Grant AUFF-E-2015-FLS-8-5, and Fonden til Lægevidenskabens Fremme Grant 19-L-0267 (to L.N. N.), a Lundbeck Foundation travel stipend Grant R296-2018-2732 to M.R.H. and Grant 8721 from the Villum Foundation to the Centre for Stochastic Geometry and Advanced Bioimaging. iPALM imaging was done in collaboration with the Advanced Imaging Center at Janelia Research Campus, a facility jointly supported by the Gordon and Betty Moore Foundation and Howard Hughes Medical Institute.

## DISCLOSURES

No conflicts of interest, financial or otherwise, are declared by the authors.

## AUTHOR CONTRIBUTIONS

M.R.H. and L.N.N. conceived and designed research; M.R.H., J.A., F.H.L., and S.R. performed experiments; M.R.H., L.G., J.A., F.H.L., and S.R. analyzed data; M.R.H., L.G., J.A., F.H.L., S.R., U.H., and L.N.N.

interpreted results of experiments; M.R.H., L.G., and J.A. prepared figures; M.R.H., L.G., and L.N.N. drafted manuscript; M.R.H., L.G., J.A., F.H.L., S.R., U.H., and L.N.N. approved final version of manuscript.

## REFERENCES

- Fenton RA, Murali SK, Moeller HB. Advances in aquaporin-2 trafficking mechanisms and their implications for treatment of water balance disorders. *Am J Physiol Cell Physiol* 319: C1–C10, 2020. doi:10.1152/ajpcell.00150.2020.
- Knepper MA, Kwon TH, Nielsen S. Molecular physiology of the water balance. *N Engl J Med* 372: 1349–1358, 2015. doi:10.1056/NEJMr1404726.
- Fushimi K, Sasaki S, Marumo F. Phosphorylation of serine 256 is required for cAMP-dependent regulatory exocytosis of the aquaporin-2 water channel. *J Biol Chem* 272: 14800–14804, 1997. doi:10.1074/jbc.272.23.14800.
- Xie L, Hoffert JD, Chou CL, Yu MJ, Pisitkun T, Knepper MA, Fenton RA. Quantitative analysis of aquaporin-2 phosphorylation. *Am J Physiol Renal Physiol* 298: F1018–F1023, 2010. doi:10.1152/ajprenal.00580.2009.
- Fenton RA, Moeller HB, Hoffert JD, Yu MJ, Nielsen S, Knepper MA. Acute regulation of aquaporin-2 phosphorylation at Ser-264 by vasopressin. *Proc Natl Acad Sci USA* 105: 3134–3139, 2008. doi:10.1073/pnas.0712338105.
- Hoffert JD, Fenton RA, Moeller HB, Simons B, Tchapyjnikov D, McDill BW, Yu MJ, Pisitkun T, Chen F, Knepper MA. Vasopressin-stimulated increase in phosphorylation at Ser269 potentiates plasma membrane retention of aquaporin-2. *J Biol Chem* 283: 24617–24627, 2008. doi:10.1074/jbc.M803074200.
- Hoffert JD, Pisitkun T, Wang G, Shen RF, Knepper MA. Quantitative phosphoproteomics of vasopressin-sensitive renal cells: regulation of aquaporin-2 phosphorylation at two sites. *Proc Natl Acad Sci USA* 103: 7159–7164, 2006. doi:10.1073/pnas.0600895103.
- Nishimoto G, Zelenina M, Li D, Yasui M, Aperia A, Nielsen S, Nairn AC. Arginine vasopressin stimulates phosphorylation of aquaporin-2 in rat renal tissue. *Am J Physiol* 276: F254–F259, 1999. doi:10.1152/ajprenal.1999.276.2.F254.
- Olesen ET, Fenton RA. Aquaporin-2 membrane targeting: still a conundrum. *Am J Physiol Renal Physiol* 312: F744–F747, 2017. doi:10.1152/ajprenal.00010.2017.
- Nielsen S, DiGiovanni SR, Christensen EI, Knepper MA, Harris HW. Cellular and subcellular immunolocalization of vasopressin-regulated water channel in rat kidney. *Proc Natl Acad Sci USA* 90: 11663–11667, 1993. doi:10.1073/pnas.90.24.11663.
- Simon H, Gao Y, Franki N, Hays RM. Vasopressin depolymerizes apical F-actin in rat inner medullary collecting duct. *Am J Physiol Cell Physiol* 265: C757–C762, 1993. doi:10.1152/ajpcell.1993.265.3.C757.
- Wen PJ, Grenklo S, Arpino G, Tan X, Liao HS, Heureaux J, Peng SY, Chiang HC, Hamid E, Zhao WD, Shin W, Näreoja T, Evergren E, Jin Y, Karlsson R, Ebert SN, Jin A, Liu AP, Shupliakov O, Wu LG. Actin dynamics provides membrane tension to merge fusing vesicles into the plasma membrane. *Nat Commun* 7: 12604, 2016. doi:10.1038/ncomms12604.
- Kanchanawong P, Shtengel G, Pasapera AM, Ramko EB, Davidson MW, Hess HF, Waterman CM. Nanoscale architecture of integrin-based cell adhesions. *Nature* 468: 580–584, 2010. doi:10.1038/nature09621.
- Shtengel G, Galbraith JA, Galbraith CG, Lippincott-Schwartz J, Gillette JM, Manley S, Sougrat R, Waterman CM, Kanchanawong P, Davidson MW, Fetter RD, Hess HF. Interferometric fluorescent super-resolution microscopy resolves 3D cellular ultrastructure. *Proc Natl Acad Sci USA* 106: 3125–3130, 2009. doi:10.1073/pnas.0813131106.
- Holst MR, Ln N. A versatile aquaporin-2 cell system for quantitative temporal expression and live-cell imaging. *Am J Physiol Renal Physiol* 317: F124–F132, 2019. doi:10.1152/ajprenal.00150.2019.
- Tingskov SJ, Choi HJ, Holst MR, Hu S, Li C, Wang W, Frøkiær J, Nejsum LN, Kwon TH, Nørregaard R. Vasopressin-independent regulation of aquaporin-2 by tamoxifen in kidney collecting ducts. *Front Physiol* 10: 948, 2019. doi:10.3389/fphys.2019.00948.
- Chen F, Tillberg PW, Boyden ES. Optical imaging. Expansion microscopy. *Science* 347: 543–548, 2015. doi:10.1126/science.1260088.
- Chozinski TJ, Halpern AR, Okawa H, Kim HJ, Tremel GJ, Wong RO, Vaughan JC. Expansion microscopy with conventional antibodies and fluorescent proteins. *Nat Methods* 13: 485–488, 2016. doi:10.1038/nmeth.3833.
- Shtengel G, Wang Y, Zhang Z, Goh WI, Hess HF, Kanchanawong P. Imaging cellular ultrastructure by PALM, iPALM, and correlative iPALM-EM. *Methods Cell Biol* 123: 273–294, 2014. doi:10.1016/B978-0-12-420138-5.00015-X.
- Myllmäki M, Mrkvicka T, Grabarnik P, Seijo H, Hahn U. Global envelope tests for spatial processes. *J R Stat Soc B* 79: 381–404, 2017. doi:10.1111/rssb.12172.
- Nedvetsky PI, Stefan E, Frische S, Santamaria K, Wiesner B, Valenti G, Hammer JA 3rd, Nielsen S, Goldenring JR, Rosenthal W, Klussmann E. A role of myosin Vb and Rab11-FIP2 in the aquaporin-2 shuttle. *Traffic* 8: 110–123, 2007. doi:10.1111/j.1600-0854.2006.00508.x.
- Arnsperg EC, Login FH, Koffman JS, Sengupta P, Nejsum LN. AQP2 plasma membrane diffusion is altered by the degree of AQP2-S256 phosphorylation. *Int J Mol Sci* 17: 1804, 2016. doi:10.3390/ijms17111804.
- Klussmann E, Tamma G, Lorenz D, Wiesner B, Maric K, Hofmann F, Aktories K, Valenti G, Rosenthal W. An inhibitory role of Rho in the vasopressin-mediated translocation of aquaporin-2 into cell membranes of renal principal cells. *J Biol Chem* 276: 20451–20457, 2001. doi:10.1074/jbc.M010270200.
- Loo CS, Chen CW, Wang PJ, Chen PY, Lin SY, Khoo KH, Fenton RA, Knepper MA, Yu MJ. Quantitative apical membrane proteomics reveals vasopressin-induced actin dynamics in collecting duct cells. *Proc Natl Acad Sci USA* 110: 17119–17124, 2013. doi:10.1073/pnas.1309219110.
- Tamma G, Klussmann E, Maric K, Aktories K, Svelto M, Rosenthal W, Valenti G. Rho inhibits cAMP-induced translocation of aquaporin-2 into the apical membrane of renal cells. *Am J Physiol Renal Physiol* 281: F1092–F1101, 2001. doi:10.1152/ajprenal.0091.2001.
- Qu L, Akbergenova Y, Hu Y, Schikorski T. Synapse-to-synapse variation in mean synaptic vesicle size and its relationship with synaptic morphology and function. *J Comp Neurol* 514: 343–352, 2009. doi:10.1002/cne.22007.
- Mironov AA, Beznoussenko GV. Models of intracellular transport: pros and cons. *Front Cell Dev Biol* 7: 146, 2019. doi:10.3389/fcell.2019.00146.
- Kuwahara M, Fushimi K, Terada Y, Bai L, Marumo F, Sasaki S. cAMP-dependent phosphorylation stimulates water permeability of aquaporin-collecting duct water channel protein expressed in *Xenopus* Oocytes. *J Biol Chem* 270: 10384–10387, 1995. doi:10.1074/jbc.270.18.10384.
- Jang KJ, Cho HS, Kang DH, Bae WG, Kwon TH, Suh KY. Fluid-shear-stress-induced translocation of aquaporin-2 and reorganization of actin cytoskeleton in renal tubular epithelial cells. *Integr Biol (Camb)* 3: 134–141, 2011. doi:10.1039/c0ib00018c.
- Moeller HB, Praetorius J, Rützler MR, Fenton RA. Phosphorylation of aquaporin-2 regulates its endocytosis and protein-protein interactions. *Proc Natl Acad Sci USA* 107: 424–429, 2010. doi:10.1073/pnas.0910683107.